A&A, 700, A274 (2025)
https://doi.org/10.1051/0004-6361/202450402
© The Authors 2025

Astronomy & Astrophysics

The source sizes of type II radio bursts with LOFAR

A. Kumari[1,2,3,⋆], D. E. Morosan[2,4], V. Mugundhan[5], P. Zhang[6,7], J. Magdalenić[8], P. Zucca[9], E. K. J. Kilpua[2], and F. Daei[2]

[1] Department of Physics, University of Helsinki, P.O. Box 64, FI-00014 Helsinki, Finland
[2] Udaipur Solar Observatory, Physical Research Laboratory, Dewali, Badi Road, Udaipur 313 001, Rajasthan, India
[3] Solar Physics Lab, NASA Goddard Space Flight Center, Greenbelt, MD 20771, USA
[4] Department of Physics and Astronomy, University of Turku, 20014 Turku, Finland
[5] Dept. of Space Planetary Astronomical Sciences and Engineering (SPASE), IITK, Kanpur 208016, India
[6] Center for Solar-Terrestrial Research, New Jersey Institute of Technology, Newark, NJ 07102, USA
[7] Cooperative Programs for the Advancement of Earth System Science, University Corporation for Atmospheric Research, Boulder, CO, USA
[8] Department of Mathematics, Faculty of Science, KU Leuven, Oude Markt 13, 3000 Leuven, Belgium
[9] ASTRON, The Netherlands Institute for Radio Astronomy, Oude Hoogeveensedijk 4, 7991 PD Dwingeloo, The Netherlands

Received 16 April 2024 / Accepted 20 June 2025

ABSTRACT

Context. Solar radio bursts can provide important insights into the underlying physical mechanisms that drive the small and large-scale eruptions on the Sun. Since metric radio observations can give us direct observational access to the inner and middle corona, they are often used as an important tool to monitor and understand the coronal dynamics.
Aims. While the sizes of the radio sources that can be observed in the solar corona are essential for understanding the nature of density turbulence within the solar corona and its subsequent influence on the angular broadening observed in radio source measurements, the smallest radio sources associated with solar radio bursts have so far been limited by observational techniques and the radio instrument's baselines.
Methods. We selected three type II bursts that were observed with the LOFAR core and remote stations in the Solar Cycle 24. We estimated the sizes and shapes (ellipticity) of the radio sources from 20–200 MHz using a two-dimensional (2D) Gaussian approximation.
Results. Our analysis shows that the smallest radio source size for type II bursts in the solar corona that can be observed in the solar atmosphere at low frequencies is 1.5′ ± 0.5′ at 150 MHz. However, even though the observations were taken with remote baselines (with a maximum distance of ∼85 km), the effective baselines were much shorter (∼15 km), likely due to snapshot imaging of the Sun.
Conclusions. Our results show that the radio source sizes are less affected by scattering than suggested in previous studies. Our measurements indicate smaller source sizes at frequencies below 95 MHz compared to previous reports, though some overlap exists with measurements at higher frequencies when using smaller baselines.

Key words. Sun: activity – Sun: corona – Sun: coronal mass ejections (CMEs) – Sun: radio radiation

1. Introduction

The coronal magnetic field plays an essential role in the formation, evolution, and dynamics of the small- and large-scale structures in the solar corona (Dulk 1970; McLean & Labrum 1985). These structures may lead to gigantic explosions in the solar atmosphere in the form of large-scale eruptions, such as coronal mass ejections (CMEs; Hundhausen 1999, and references therein) that may severely impact near-Earth space. CMEs can reach Earth within several hours to days, and, depending on the orientation of its internal magnetic field, they can interact with the Earth's magnetosphere to cause severe geomagnetic storms (Gosling et al. 1990; Kilpua et al. 2014). Moreover, the shocks generated by CMEs can accelerate the energetic particles leading to highly energetic solar radiation storms (e.g. Cane & Stone 1984; Morosan et al. 2024). These eruptions are often accompanied by radio emissions called solar radio bursts (SRBs; Kundu & Stone 1984). Radio emission can be generated either by electrons accelerated during the eruption or thermal electrons interacting with the background plasma (e.g. Morosan et al. 2019a). These emissions can be observed with ground- and space-based observatories. Radio observations are one of the most common approaches to diagnosing non-thermal electrons in the solar atmosphere (Maia et al. 2000; Carley et al. 2020; Chrysaphi et al. 2020; Majumdar et al. 2021).

One direct signature of CME-driven shocks at radio wavelengths is known as metric type II radio bursts (Roberts 1959; Smerd et al. 1975; Kumari et al. 2017a; Morosan et al. 2023). Type II bursts originate from plasma waves converted into radio waves at the local plasma frequency and/or its harmonics. These radio bursts can be considered a direct diagnosis of MHD shocks in the solar atmosphere. These bursts can be used to study the kinematics, energetics, and dynamics of the associated eruptive events very close to the Sun (Mancuso & Raymond 2004; Kumari et al. 2017b; Morosan et al. 2019b; Kandekar & Kumari 2025). Radio sources can provide important insights into the underlying physical mechanisms that drive the small- and large-scale eruptions on the Sun (Gopalswamy et al. 2013; Chen et al. 2014; Kumari et al. 2019; Chrysaphi et al. 2018; Morosan et al.

⋆ Corresponding author: anshu@prl.res.in

Open Access article, published by EDP Sciences, under the terms of the Creative Commons Attribution License (https://creativecommons.org/licenses/by/4.0), which permits unrestricted use, distribution, and reproduction in any medium, provided the original work is properly cited.
This article is published in open access under the Subscribe to Open model. Subscribe to A&A to support open access publication.

2021; Zucca et al. 2025). Several studies have shown that the radio source shapes, sizes, and evolution can be used to probe plasma turbulence in the solar corona (Mugundhan et al. 2017; Kontar et al. 2017). However, the smallest radio sources that can be observed in the solar corona have been less explored due to several observational challenges (Bastian 1994; Thejappa & MacDowall 2008). At metric wavelengths, practically speaking it is difficult to obtain arcsecond spatial resolutions (comparable to visible wavelengths) due to the need for larger baselines of radio interferometers (Monnier & Allen 2013) and irregular refraction of radio waves in the solar corona due to turbulence (Kuznetsov et al. 2020). There have been a few occultation observations during solar eclipses at frequencies below 200 MHz, where the results indicate that sources sizes of ∼1′ can be observed in the solar atmosphere (Letfus et al. 1967; Kathiravan et al. 2011). Hence, the largest baselines required for imaging the active Sun at frequencies ≤200 MHz needs to be investigated (Aubier et al. 1971; Schmahl et al. 1994; Bastian 2004) to obtain concrete information about the size of radio sources observed in the solar corona.

With the recent advancement in the low-frequency radio instruments (both solar and non-solar dedicated) such as the Mingantu Spectral Radio Heliograph (MUSER; Yan et al. 2021), the LOw Frequency ARray (LOFAR; van Haarlem et al. 2013), the Murchison Widefield Array (MWA; Tingay et al. 2013), and the upgraded Giant Metrewave Radio Telescope (GMRT; Gupta et al. 2017), it is possible to observe the Sun at low frequencies with arcsecond angular resolutions. There have been a few studies in the past to determine the source sizes of radio bursts with these radio interferometers. Zhang et al. (2020) studied the fundamental and harmonic emissions from a type III burst using interferometric observations with LOFAR and found that the source sizes were ∼25′ at 26.5 MHz. Recently, Dabrowski et al. (2023) studied type IIIb and U solar bursts with LOFAR as well. Previously, Mercier et al. (2006) combined two radio interferometers, GMRT in India and the Nançay Radioheliograph (NRH; Kerdraon & Delouis 1997) in France, and obtained the source size of ∼1′ at 326 MHz for solar noise storms. (Gordovskyy et al. 2022) studied nine radio bursts (including two type II bursts) with LOFAR's tied-array beam mode. They used empirical methods to remove instrumental and ionospheric effects on the source sizes and found that the sizes can be 5′−30′ from 45–30 MHz. The smallest source size that has been reported at low frequencies by interferomteric observations is ∼15″, reported by Mugundhan et al. (2018a) at 55 MHz. Several other authors have also reported the source sizes to be ∼15−30′ between 100 and 10 MHz (Zhang et al. 2020; Murphy et al. 2021). However, almost all these studies are focused on solar noise storms or type III radio bursts. A recent interferometric study showed that increasing the baselines of radio observations and, thus, increasing the spatial resolution, reveals new details of radio images of type II bursts, where an elongated single radio source in low-resolution images is in fact composed of two separate neighbouring sources in high-resolution images (Morosan et al. 2025). Thus, it is important to quantify the size of radio sources in the case of type II bursts in the solar corona.

In this work, we took advantage of LOFAR's combined core (24 stations) and remote (14 stations) baselines – with a capability of providing a maximum baseline of ∼84 km – to study type II radio source sizes and their shapes. For this, we used the LOFAR observations for three type II bursts: (i) August 25, 2014; (ii) October 16, 2015 (A); and (iii) October 16, 2015 (B). This article is organised as follows: Sect. 2 describes the LOFAR interferometric observations of these events; Sect. 3 contains the data analysis methods and results; and in Sect. 4 we discuss the results and conclude the article.

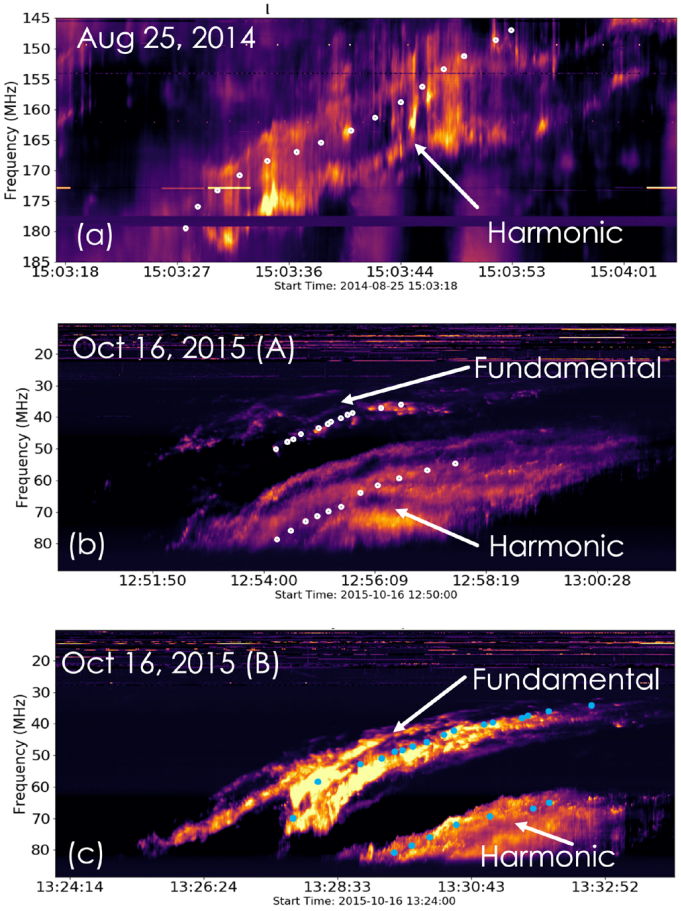

Fig. 1. Dynamic spectra of (a) harmonic band of type II burst observed with HBA of LOFAR on August 25, 2014; (b) F-H of type II bursts observed with LBA of LOFAR on October 16, 2015 (A) (the upper part of the spectra (HBA) is not shown here); (c) same as (b), but for October 16, 2015 (B) event. The arrow shows the F-H bands of these type II bursts. The white and cyan marks are the time frequency at which interferometric radio imaging was carried out and are shown in subsequent figures in this article. The imaging time and frequency were chosen in such a way to cover both fundamental and harmonic bands of type II bursts (if available).

2. Data and observation

2.1. Event 1: August 25, 2014

A fundamental-harmonic (F-H) type II burst was observed with LOFAR on August 25, 2014 in both bands, high-band antennae (HBA; 110–240 MHz), and low-band antennae (LBA; 10–90 MHz) (van Haarlem et al. 2013). The start and end frequencies of this type II burst were ≈170 MHz (≈15:01 UT) and ≈20 MHz (≈15:31 UT), respectively. Though LOFAR operates in spectral mode for both LBA and HBA, at present, the interferometric observations are only in one of the bands. For this type II burst, the interferometric imaging observations were taken with the HBA, which corresponds to the harmonic band. The dynamic spectra for the HBA band are shown in Fig. 1(a).

Table 1. Details of the three type II radio bursts' interferometric observations with LOFAR.

Date	Details	Frequency (MHz)		Time (UT)		Imaging		Feature	
		Start	End	Start	End	LBA	HBA	F	H
25/08/2024	F-H	170	20	15:01	15:31	N	Y	N	Y
16/10/2015 (A)	F-H	178	30	12:51	13:01	Y	N	Y	Y
16/10/2015 (B)	F-H	169	33	13:25	13:34	Y	N	Y	Y

2.2. Event 2: October 16, 2015 (A)

Another F-H type II burst was observed with both LOFAR bands – HBA and LBA – on October 16, 2015. The start and end frequencies of this type II burst were ≈178 MHz (≈12:51 UT) and ≈30 MHz (≈13:01 UT), respectively. For this type II burst, the interferometric imaging observations were taken with the LBA, which had both of the F-H bands. The dynamic spectra for the LBA band is shown in Fig. 1(b). There was another type II burst on the same day; hence, we refer to this event as October 16, 2015(A) hereafter.

2.3. Event 3: October 16, 2015 (B)

The third type II burst was observed on October 16, 2015 with both HBA and LBA bands of LOFAR. This was also an F-H pair. The start and end frequencies of this type II burst were ≈169 MHz (≈13:25 UT) and ≈33 MHz (≈13:25 UT), respectively. For this type II burst, the interferometric imaging observations were taken with the LBA, which had both of the F-H bands. The dynamic spectra for the LBA band is shown in Fig. 1(c). We refer to this event as October 16, 2015(B) hereafter.

For August 25, 2014, the interferometric observations were obtained with 24 core stations and 12 remote stations, which provided 595 cross-correlation baselines in total. Two sub-array-pointing beams were configured to observe the Sun (target) and Taurus-A (calibrator). For October 16, 2015, the interferometric observations were obtained with 23 core stations and 12 remote stations, which provided a total of 561 cross-correlation baselines. Two sub-array pointings were configured to observe the Sun (target) and Virgo-A (calibrator). The temporal and spectral resolution of these interferometric observations were 0.25 s and 195.3 kHz, respectively. This high resolution unique LOFAR interferometric observation provided high-time and -frequency-resolution images of both F-H bands in the type II burst as well as the possibility to estimate the radio source sizes across the observed frequency ranges. The first event was studied in more detail by Magdalenić et al. (2020), where the authors considered the fine structure of this type II burst. The second event was studied from the shock origin point by Maguire et al. (2021), where the authors found that the type II burst originated from a jet-driven piston shock. In the present paper, we report the type II source sizes and shapes for these events.

3. Data analysis and results

We determined the locations and source sizes of the type II bursts (both F-H ones, if available) using the LOFAR interferometric observations. The dots marked in Fig. 1 are the time-frequency points for which we performed radio imaging during these three events. For event 1 (August 25, 2014) and events 2 and 3 (October 16, 2015), the calibrators were Turaus A and Virgo A, respectively. We selected radio frequency interference (RFI)-free bands for imaging. We used the Default Pre-Processing Pipeline (DPPP) for interferometric imaging (van Diepen et al. 2018). Table 1 shows the LOFAR bands and type II sources that were imaged from these datasets.

The low frequency array provides the raw visibility data in the form of measurement sets (MSs) (van Haarlem et al. 2013). An MS is structured as a directory containing tables and sub-directories storing both data and metadata (McMullin et al. 2007). The primary table includes information such as the (u,v,w) coordinates in its UVW column, which are essential for correlating data from different antennas. Initially, we conducted a manual inspection of the raw visibilities to identify and flag bad channels, antennas, and baselines. Following this, calibration procedures were applied using the observed calibrators specific to each event (see previous paragraph for details). The pre-processing and calibration were done using the Default Pre-Processing Pipeline (DPPPP) tool as described in van Diepen et al. (2018). These calibration steps involved correcting for amplitude, phase, and bandpass variations across the observed frequencies. Once calibrated, the WSCLEAN algorithm was employed for further data processing (Offringa et al. 2014). WSCLEAN performs image-domain de-convolution utilising the CLEAN algorithm and subsequently restores the images from the calibrated visibility data. This iterative process was used to enhance the signal-to-noise (S/N) while preserving the spatial resolution necessary for detailed imaging of the radio burst.

Figure 2 shows the location of the type II bursts from this study. We estimated the source sizes and its positions using a 2D Gaussian fit for calibrated and corrected solar images. The source sizes were calculated using 2D Gaussian fits, and then errors were estimated again using the maximum brightness temperature, noise floor, and beam sizes at different frequencies (see e.g. the methods used in Morosan et al. 2019b). The x and y extent bars in Fig. 2 denote the size of the source in the major and minor axis directions, respectively, while the error bars in Fig. 3 denote the uncertainty in source sizes following the Gaussian fit.

We fitted a power-law equation to estimate the frequency dependence of the source sizes on the solar atmosphere. The power-law exponent for the major axis varied, with values of ≈1.5 for harmonic and ≈0.75 for fundamental sources. In Fig. 3, we show the source sizes estimated for all three events analysed in this study, along with their corresponding power-law exponents for both minor and major axes. Our results indicate that for fundamental lanes associated with type II bursts, estimated source sizes range from 1–5′ for the frequency range 30–70 MHz. In contrast, for harmonic sources, sizes varied around ≈1′ and ≈2′ at higher (180–145 MHz) and lower LOFAR bands (85–55 MHz), respectively. These sizes slightly exceed the beam sizes observed at these frequencies during interferometric observations with LOFAR using the antenna set of core plus remote array with the longest baseline of ≈13 km.

For the minor axis, fundamental source sizes ranged from ≈2–5′, while harmonic sources were approximately ≈2′ in size. Notably, the source sizes in both major and minor axis

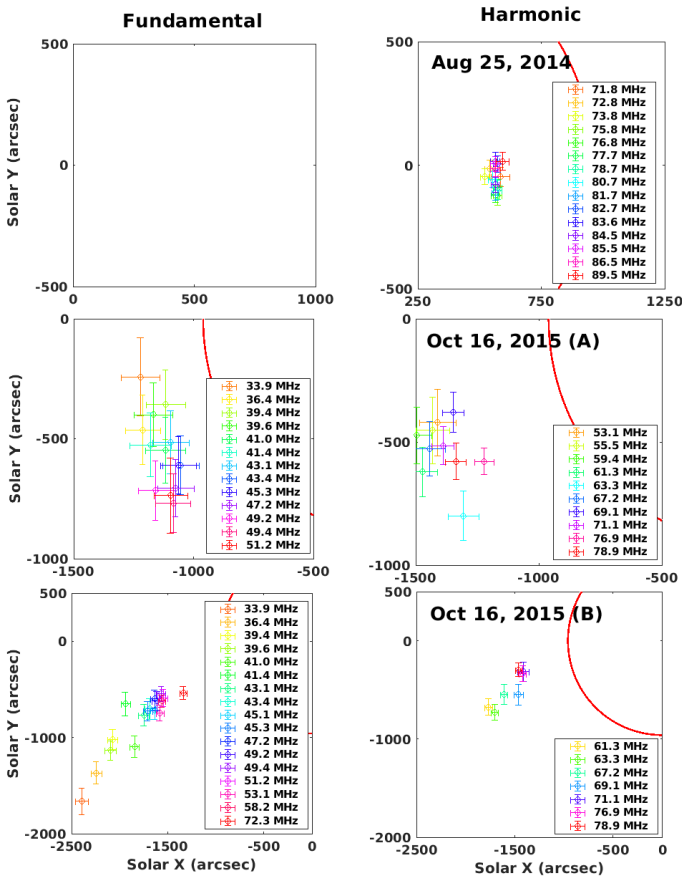

Fig. 2. Centroid location of type II radio burst sources for all the three events studied in the present work (row-wise). The fundamental and harmonic radio sources are plotted column-wise. The extent of these sources in the major and minor directions is represented by the bars centered on each centroid in the x and y directions, respectively. The red circles show the visible Sun. Since there was no interferometric observation for the fundamental band of the first type II, we have images for the harmonic band only. These images correspond to the white and cyan marks on the three spectra shown in Fig. 1.

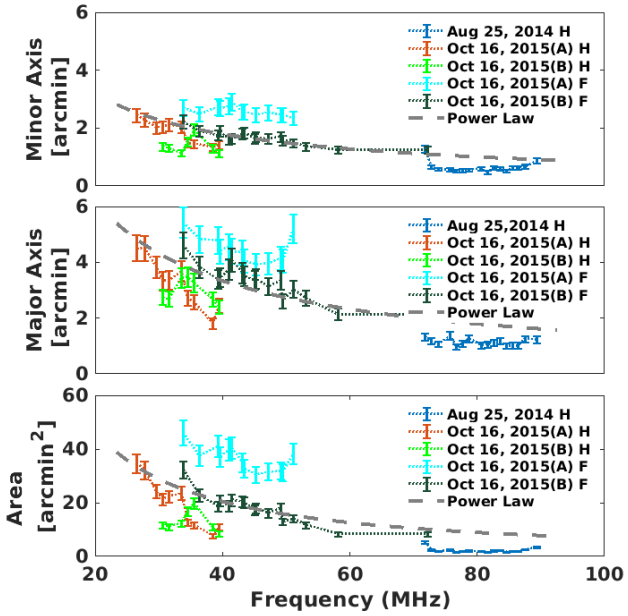

Fig. 3. Sizes (major and minor extent [1/e]) and area of radio sources for all three type II bursts studied in the present work: (a) radio sources extended in equatorial direction; (b) radio sources extended in polar direction; (c) area of the radio sources. Different events and data corresponding to their features are shown in different colors. The grey dashed line is a combined power-law fit to the data. The error bars denote the uncertainty in source sizes following the Gaussian fit to the radio sources to estimate their sizes.

directions were significantly bigger than the beam size in the EW direction during interferometric observations, suggesting limitations imposed by baseline distance or snapshot imaging where not enough signal would have been detected by the farther away remote stations in the limited time frame. Mugundhan et al. (2018b) reported source sizes as low as ≈15″ at 53 MHz; compared to this, we obtained almost ≈8× bigger sizes, and one of the reasons for that is the presence of smaller baselines. Another reason for out result could be the high level of solar activity at the time of the studied events, during which we expect scattering effects to be more pronounced. While comparing these source sizes obtained with interferometric observations to the scattering removed tied-array beam observation by Gordovskyy et al. (2022), we report significantly lower source sizes for type II bursts observed with LOFAR's interferometric mode.

4. Discussion and summary

The smallest angular dimensions of compact radio sources in the solar atmosphere that can be observed still represent an open question. As has been evident with large baseline radio instruments, many small sources can be observed. The radio source sizes play a crucial role in our understanding of the dynamics of density turbulence within the solar corona – especially at low frequencies – and its effect on the angular extent of radio sources. The extent of the interferometric baselines necessary to observe radio sources in the solar atmosphere must be sufficiently large to put a constrain on the observable smallest compact radio source. The 2D geometry of low-frequency radio sources and their frequency dependence has been under-explored due to the limited spatial resolution of radio imaging telescopes.

Here, we present a comprehensive study of multiple type II radio bursts across various frequency bands, to understand their source characteristics. We analysed source shapes by approximating the derived intensity distributions through the application of 2D Gaussian profiles using elliptical 1/e contours. The three events shown here had fundamental and/or harmonic imaging observations available from LOFAR. In our studies, we looked into the shape and sizes of these radio bursts. The sizes of the radio sources were estimated by the extent of the source, which depends on several factors including the peak brightness, root mean square (rms) noise floor, and beam size at each frequency. We note that source sizes can also vary on sub-second (≈100 ms) scales. In the current study, we focused on the variation of source characteristics with frequency across different events rather than on temporal variations on sub-second scales.

Figure 2 indicates that in the case of event 3 and clearly radially outward-propagating radio sources (i.e. approximately along the radially stretching magnetic field lines; see panels (e) and (f)), the obtained radio source sizes are rather small and compact. In the case of event 2, the positions of the radio sources at subsequent frequencies indicate shockwave propagation towards the observer under an angle of <90° (see panels (c) and (d)), indicating that the large spread of radio source sizes could result from the radio emission propagating in the region with the complex configuration of the magnetic field. On the

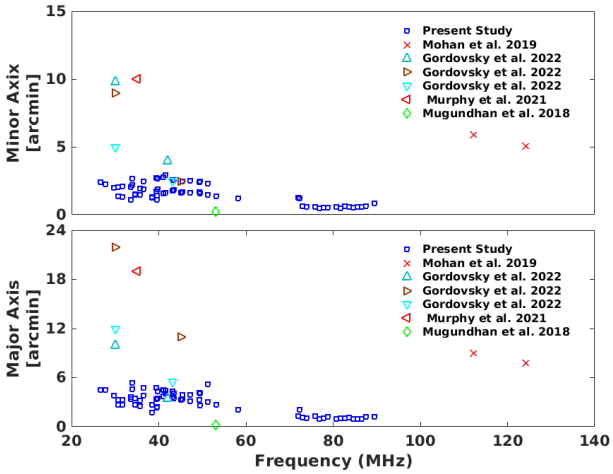

Fig. 4. Combined plot of source sizes with various previous studies. Blue squares are the source sizes for F-H lanes of three type II radio bursts studied in the present case. Notably, the source sizes (both minor and major) obtained in the present study is smaller than all the previous studies with different instruments and different modes of observations (except Mugundhan et al. 2018a).

other hand, very compact and almost completely superposed radio source positions in the case of event 1 indicate type II bursts propagate fully along the Sun-Earth line. However, we note that without having 3D radio source positions, we can only conclude that the obtained trajectories and the radio source sizes for studied events indicate both different scattering effects and possibly different orientation of the underlying coronal magnetic field.

Figure 4 shows a combined plot of some of the previous studies when compared to the results obtained with the present one. We compared our results with the type II bursts observed with LOFAR tied-array beam observations of type II radio bursts (Gordovskyy et al. 2022), type III bursts observed with MWA (Mohan et al. 2019), type III radio burst observations with the interferometric mode of LOFAR (Murphy et al. 2021), and very long baseline interferometry (VLBI) of a noise storm (Mugundhan et al. 2018a). Notably, the source sizes obtained in the present study are smaller than those of previous studies, except that of Mugundhan et al. (2018a), where the baseline was ≈200 km.

When comparing our findings with those of Gordovskyy et al. (2022), which is the only other study available that analysed type II source sizes, a disparity was noticed: the observed sources in the present study exhibit significantly smaller dimensions, without the application of any scattering removal techniques. Despite this discrepancy, both our results and those of Gordovskyy et al. (2022) align with models of anisotropic radio-wave scattering within the solar corona when using different scattering parameters to determine the level of turbulence (e.g. Kontar et al. 2023). In comparison with other LOFAR observations, the source sizes in the present study have smaller areas than those reported by Dabrowski et al. (2023) for type III radio bursts, which also used LOFAR's interferometric mode in a similar configuration. Further studies are thus necessary to quantify if scattering effects are generally larger for type III bursts compared to type II bursts or if these effects change significantly with solar activity.

Previously, Mugundhan et al. (2018b) demonstrated that the type III radio bursts' source sizes, during periods of solar cycle minima, can be as small as ≈15″. The authors connected this effect to the smaller impact of the scattering processes on the radio source sizes at the time of the low-level solar activity when the radio emission propagates through less structured coronae. We note that LOFAR observations in the present study were made during the solar maximum phase. It is important to note that radio scattering is inherently anisotropic, which can influence observed source sizes (Kontar et al. 2023). This anisotropy, alongside other scattering effects, may contribute to the broadening of solar radio sources and should be considered when interpreting size measurements. Despite this, our present findings indicate notably smaller radio source sizes than previously reported. This could imply the following three different scenarios.

1. Scattering effects are generally smaller than previously expected.
2. As the source would be embedded in the scattering medium itself, scattering could happen much closer to the vicinity of the source itself, resulting in the spherical waves from source being scattered, rather than plane waves, which could result in smaller angular sizes (Subramanian & Cairns 2011).
3. The level of the scattering experienced by the radio emission is depending not only on the density inhomogeneities of the ambient corona (Jebaraj et al. 2023) but also on the orientation of the underlying magnetic field.

Figure 3(c) shows that the area of the radio sources for the type II bursts studied in the present study matches closely with those from simulations by Clarkson & Kontar (2025), which found ≈29.7 arcmin^2 in non-radial magnetic fields. We note that similar source sizes were also reported in a different study for herringbones found in a type II burst (Zhang et al. 2024). Future high-resolution interferometric observations, during different stages of solar activity, have the potential to further constrain these intrinsically complex problems.

Acknowledgements. A.K., D.E.M. and P.Z. acknowledge the University of Helsinki Three Year Grant. A.K is supported by an appointment to the NASA Postdoctoral Program at the NASA Goddard Space Flight Center (GSFC). AK acknowledges the ANRF Prime Minister Early Career Research Grant (PM ECRG) program. D.E.M acknowledges the Academy of Finland project 'RadioCME' (grant number 333859) and Academy of Finland project 'SolShocks' (grant number 354409). E.K.J.K. and A.K. acknowledge the European Research Council (ERC) under the European Union's Horizon 2020 Research and Innovation Programme Project SolMAG 724391. E.K.J.K acknowledges the Academy of Finland Project SMASH 310445. All authors acknowledge the Finnish Centre of Excellence in Research of Sustainable Space (Academy of Finland grant number 312390). The authors wish to acknowledge CSC – IT Center for Science, Finland, for computational resources. This paper is based on data obtained with LOFAR (van Haarlem et al. 2013), which is the Low Frequency Array designed and constructed by ASTRON. This research used version 4.1 (The SunPy Community et al. 2020) of the SunPy open source software package and version R2018b (The MathWorks Inc. 2018) of MATLAB.

References

Aubier, M., Leblanc, Y., & Boischot, A. 1971, A&A, 12, 435
Bastian, T. S. 1994, ApJ, 426, 774
Bastian, T. S. 2004, Planet. Space Sci., 52, 1381
Cane, H. V., & Stone, R. G. 1984, ApJ, 282, 339
Carley, E. P., Baldovin, C., Benthem, P., et al. 2020, J. Space Weather Space Clim., 10, 7
Chen, Y., Du, G., Feng, L., et al. 2014, ApJ, 787, 59
Chrysaphi, N., Kontar, E. P., Holman, G. D., & Temmer, M. 2018, ApJ, 868, 79
Chrysaphi, N., Reid, H. A. S., & Kontar, E. P. 2020, ApJ, 893, 115
Clarkson, D. L., & Kontar, E. P. 2025, ApJ, 978, 73
Dabrowski, B., Mikuła, K., Flisek, P., et al. 2023, A&A, 669, A52
Dulk, G. A. 1970, Pub. Astron. Soc. Austrl., 1, 308
Gopalswamy, N., Xie, H., Mäkelä, P., Yashiro, S., & Akiyama, S. 2013, Adv. Sp. Res., 51, 1981

Gordovskyy, M., Kontar, E. P., Clarkson, D. L., Chrysaphi, N., & Browning, P. K. 2022, ApJ, 925, 140
Gosling, J. T., Bame, S. J., McComas, D. J., & Phillips, J. L. 1990, Geophys. Res. Lett., 17, 901
Gupta, Y., Ajithkumar, B., Kale, H. S., et al. 2017, Curr. Sci., 113, 707
Hundhausen, A. 1999, in The Many Faces of the Sun, 143
Jebaraj, I. C., Magdalenic, J., Krasnoselskikh, V., Krupar, V., & Poedts, S. 2023, A&A, 670, A20
Kandekar, J., & Kumari, A. 2025, A&A, 697, L9
Kathiravan, C., Ramesh, R., Barve, I. V., & Rajalingam, M. 2011, ApJ, 730, 91
Kerdraon, A., & Delouis, J. M. 1997, in The Nançay Radioheliograph, ed. G. Trottet, 483, 192
Kilpua, E. K. J., Mierla, M., Zhukov, A. N., et al. 2014, Sol. Phys., 289, 3773
Kontar, E. P., Yu, S., Kuznetsov, A. A., et al. 2017, Nat. Commun., 8, 1515
Kontar, E. P., Emslie, A. G., Clarkson, D. L., et al. 2023, ApJ, 956, 112
Kumari, A., Ramesh, R., Kathiravan, C., & Wang, T. J. 2017a, Sol. Phys., 292, 161
Kumari, A., Ramesh, R., Kathiravan, C., & Gopalswamy, N. 2017b, ApJ, 843, 10
Kumari, A., Ramesh, R., Kathiravan, C., Wang, T. J., & Gopalswamy, N. 2019, ApJ, 881, 24
Kundu, M. R., & Stone, R. G. 1984, Adv. Space Res., 4, 261
Kuznetsov, A. A., Chrysaphi, N., Kontar, E. P., & Motorina, G. 2020, ApJ, 898, 94
Letfus, V., Tlamicha, A., & Valníček, B. 1967, Sol. Phys., 1, 474
Magdalenić, J., Marqué, C., Fallows, R. A., et al. 2020, ApJ, 897, L15
Maguire, C. A., Carley, E. P., Zucca, P., Vilmer, N., & Gallagher, P. T. 2021, ApJ, 909, 2
Maia, D., Pick, M., Vourlidas, A., & Howard, R. 2000, ApJ, 528, L49
Majumdar, S., Tadepalli, S. P., Maity, S. S., et al. 2021, Sol. Phys., 296, 62
Mancuso, S., & Raymond, J. C. 2004, A&A, 413, 363
McLean, D. J., & Labrum, N. R. 1985, Solar radiophysics: studies of emission from the sun at metre wavelengths (New York: Cambridge University Press)
McMullin, J. P., Waters, B., Schiebel, D., Young, W., & Golap, K. 2007, in Astronomical Data Analysis Software and Systems XVI, eds. R. A. Shaw, F. Hill, & D. J. Bell, Astronomical Society of the Pacific Conference Series, 376, 127
Mercier, C., Subramanian, P., Kerdraon, A., et al. 2006, A&A, 447, 1189
Mohan, A., Mondal, S., Oberoi, D., & Lonsdale, C. J. 2019, ApJ, 875, 98
Monnier, J. D., & Allen, R. J. 2013, in Astronomical Techniques, Software and Data, eds. T. D. Oswalt, & H. E. Bond, Planets, Stars and Stellar Systems, 2, 325
Morosan, D. E., Kilpua, E. K. J., Carley, E. P., & Monstein, C. 2019a, A&A, 623, A63
Morosan, D. E., Carley, E. P., Hayes, L. A., et al. 2019b, Nat. Astron., 3, 452
Morosan, D. E., Kumari, A., Kilpua, E. K. J., & Hamini, A. 2021, A&A, 647, L12
Morosan, D. E., Pomoell, J., Kumari, A., Kilpua, E. K. J., & Vainio, R. 2023, A&A, 675, A98
Morosan, D. E., Pomoell, J., Palmroos, C., et al. 2024, A&A, 683, A31
Morosan, D. E., Jebaraj, I. C., Zhang, P., et al. 2025, A&A, 695, A70
Mugundhan, V., Hariharan, K., & Ramesh, R. 2017, Sol. Phys., 292, 155
Mugundhan, V., Ramesh, R., Kathiravan, C., et al. 2018a, ApJ, 855, L8
Mugundhan, V., Ramesh, R., Kathiravan, C., Gireesh, G. V. S., & Hegde, A. 2018b, Sol. Phys., 293, 41
Murphy, P. C., Carley, E. P., Ryan, A. M., Zucca, P., & Gallagher, P. T. 2021, A&A, 645, A11
Offringa, A. R., McKinley, B., Hurley-Walker, N., et al. 2014, MNRAS, 444, 606
Roberts, J. A. 1959, Aust. J. Phys., 12, 327
Schmahl, E. J., Gopalswamy, N., & Kundu, M. R. 1994, Sol. Phys., 150, 325
Smerd, S. F., Sheridan, K. V., & Stewart, R. T. 1975, Astrophys. Lett., 16, 23
Subramanian, P., & Cairns, I. 2011, J. Geophys. Res.: Space Phys., 116, A03104
The MathWorks Inc. 2018, MATLAB version: 9.5.0.944444 (R2018b) (Natick, Massachusetts, United States: The MathWorks Inc.)
The SunPy Community, Barnes, W. T., Bobra, M. G., et al. 2020, ApJ, 890, 68
Thejappa, G., & MacDowall, R. J. 2008, ApJ, 676, 1338
Tingay, S. J., Goeke, R., Bowman, J. D., et al. 2013, PASA, 30, e007
van Diepen, G., Dijkema, T. J., & Offringa, A. 2018, Astrophysics Source Code Library [record ascl:1804.003]
van Haarlem, M. P., Wise, M. W., Gunst, A. W., et al. 2013, A&A, 556, A2
Yan, Y., Chen, Z., Wang, W., et al. 2021, Front. Astron. Space Sci., 8, 20
Zhang, P., Zucca, P., Sridhar, S. S., et al. 2020, A&A, 639, A115
Zhang, P., Morosan, D., Kumari, A., & Kilpua, E. 2024, A&A, 683, A123
Zucca, P., Zhang, P., Kozarev, K., et al. 2025, A&A, submitted [arXiv:2505.12932]

Appendix A: Raw images and visibilities

To ensure potential over-cleaning, we took several precautions to ensure the quality of our images:

- Thresholding: We carefully set the cleaning threshold to maintain the maximum brightness in the corrected data above the noise floor. This approach helps prevent over-cleaning while preserving faint signal details, consistent with standard practices in radio astronomy imaging tools such as AIPS, CASA, and WSClean.
- Signal-to-noise ratio control: We systematically monitored the S/N throughout the cleaning process to avoid cleaning at or below the noise level, which would risk over-cleaning the data.
- Cleaning algorithm: We employed the CLEAN algorithm originally developed by Högbom (1974), specifically using the WSClean implementation by Offringa et al. (2014). This method has been widely adopted for over five decades in radio astronomy for its effectiveness in reconstructing complex source structures. Its reliability and robustness are well established within the community.

Recent studies (Morosan et al. 2025) have shown that increasing the baseline lengths in solar radio imaging of type II bursts results in higher image resolution and decreased source sizes, which remain larger than the WSClean restoring beam. Below we provide a sample calibrated image in the RA–Dec coordinate system. The peak brightness reaches approximately 10^9 K, while the residual noise level is around 10^5 K, resulting in a S/N of about 40 dB.

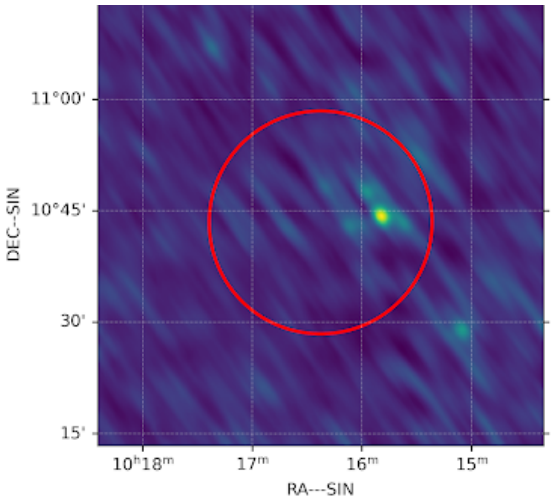

Fig. A.1. Raw radio image (corrected for phase, amplitude, and bandpass effects, but not cleaned) shown in the RA–Dec coordinate system for 165 MHz on August 25, 2014 at 15:04:11 UT. The red circle represents the solar photosphere.

In addition to image-domain analysis, we also examined the raw visibility data to ensure that the source sizes inferred from the interferometric images are consistent with the UV-distance behavior, both during quiet and active Sun conditions.

In these visibility plots, we observe that the quiet Sun visibility amplitudes drop close to the noise floor at UV distances of approximately 5 km. In contrast, for the radio bursts associated with the type II event, the visibility amplitudes reach the noise floor only at baselines of approximately 13 km. This clearly indicates that compact structures with sizes as small as $\sim 0.5''$ are present at the higher frequencies during the type II emission, consistent with the sizes inferred from the interferometric images presented in this study.

Moreover, since our analysis involves a large number of images generated through a semi-automated imaging pipeline, it is more straightforward and efficient to handle the cleaned image products rather than examining the visibility amplitudes for each time and frequency point individually.

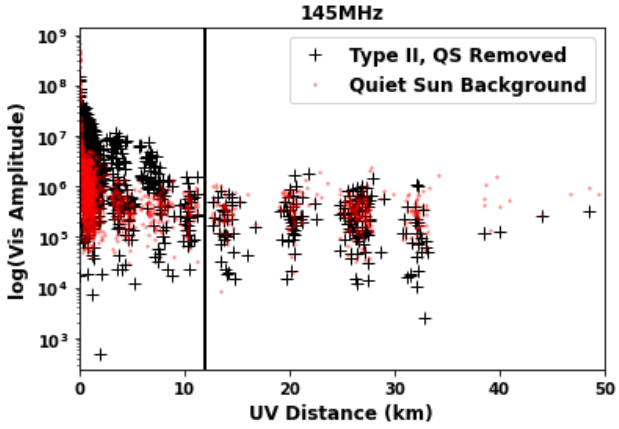

Fig. A.2. Visibility amplitudes versus UV distance for type II bursts (black) and quiet Sun images (red). Here, the quiet Sun is averaged over 2 minutes to enhance the contrast. After the black curve flattens, the excess flux arises from increased noise due to the shorter (20-second) integration during the burst.

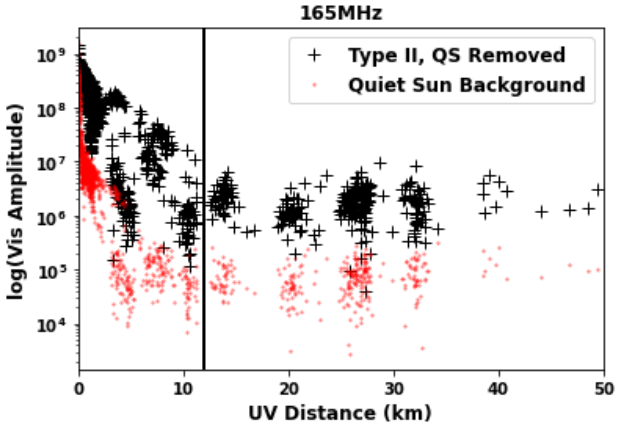

Fig. A.3. Same as Fig. A.2 but at 165 MHz.